

000
001
002
003
004
005
006
007
008
009
010
011
012
013
014
015054
055
056
057
058
059
060
061
062
063
064
065
066
067
068
069
070
071
072
073
074
075
076
077
078
079
080
081
082
083
084
085
086
087
088
089
090
091
092
093
094
095
096
097
098
099
100
101
102
103
104
105
106
107

Learning a More Continuous Zero Level Set in Unsigned Distance Fields through Level Set Projection

Anonymous ICCV submission

Paper ID 6311

Abstract

Latest methods represent shapes with open surfaces using unsigned distance functions (UDFs). They train neural networks to learn UDFs and reconstruct surfaces with the gradients around the zero level set of the UDF. However, the differential networks struggle from learning the zero level set where the UDF is not differentiable, which leads to large errors on unsigned distances and gradients around the zero level set, resulting in highly fragmented and discontinuous surfaces. To resolve this problem, we propose to learn a more continuous zero level set in UDFs with level set projections. Our insight is to guide the learning of zero level set using the rest non-zero level sets via a projection procedure. Our idea is inspired from the observations that the non-zero level sets are much smoother and more continuous than the zero level set. We pull the non-zero level sets onto the zero level set with gradient constraints which align gradients over different level sets and correct unsigned distance errors on the zero level set, leading to a smoother and more continuous unsigned distance field. We conduct comprehensive experiments in surface reconstruction for point clouds, real scans or depth maps, and further explore the performance in unsupervised point cloud upsampling and unsupervised point normal estimation with the learned UDF, which demonstrate our non-trivial improvements over the state-of-the-art methods.

1. Introduction

Surface reconstruction from point clouds plays an important role in vision, robotics and graphics. Recently, neural implicit functions [43, 40, 39] have achieved remarkable results by representing 3D geometries with signed distance functions (SDFs) [36, 12, 53], occupancy [39, 46, 42] or unsigned distance functions (UDFs) [62, 15, 21]. SDFs and occupancy explore the internal-to-external relations, which are limited to reconstruct closed surfaces. Researchers therefore turn to UDFs, which is a more general function,

to represent shapes with arbitrary typologies.

Learning an accurate zero level set of UDF is the key factor for representing complex geometries and supporting 3D applications [37, 29, 20]. However, the differential neural networks struggle from learning the zero level set where the UDF is not differentiable. This leads to unstable optimizations, which results in large errors on unsigned distances and gradients around the zero level set, causing failures in downstream 3D applications. Taking surface reconstruction for example, SOTA methods [62, 21] extract surfaces from UDFs by judging gradient directions around the zero level set, where the unreliable gradients lead to highly fragmented and discontinuous surfaces.

To resolve this issue, we introduce two novel constraints on the zero level set in forms of losses for learning accurate UDF without ground truth unsigned distances. The key insight is from the observation that despite the unreliable zero level set, the non-zero level sets learned by UDF are quite convincing, which can serve as an accurate guidance for the optimization on zero level set. We therefore propose the level set projection constraint to achieve a smoother and more continuous zero level set of UDF by enforcing the parallelism between the gradient of a query in a non-zero level set and the gradient of its projection to the zero level set. Moreover, we introduce an adaptive weighting strategy to force the neural network to focus more on the optimization nearer to the zero level set.

The level set projection constraint aims to guide the gradients at zero level set, where we propose another unsigned distance loss as a supplement for correcting distance errors at the zero level set. To bring a more robust guidance to the optimization of zero level set, we introduce an addition gradient constraint on queries to learn more accurate and regular non-zero level sets of UDF by encouraging the gradient orthogonal to the tangent plane of the surface.

Based on our learned stable UDF with an accurate zero level set, we explore three different 3D applications, including surface reconstruction, unsupervised point normal estimation and unsupervised point cloud upsampling. Our improvements over unsupervised or even supervised baselines

108 justify both our effectiveness and the importance of an
 109 accurate and continuous zero level set to the representation
 110 ability of neural unsigned fields.
 111

112 Our main contributions can be summarized as follows.
 113

- 114 • We propose two novel constraints on UDF to achieve a
 115 smoother and more continuous zero level set for learning
 116 to represent shapes or scenes without ground truth
 117 unsigned distances.
 118
- 119 • We justify that an accurate and continuous zero level
 120 set is the key factor to represent complex 3D geometries
 121 and supporting 3D downstream applications.
 122
- 123 • We explore three different 3D applications with our
 124 learned UDF, including surface reconstruction, unsupervised
 125 point normal estimation and unsupervised point cloud
 126 upsampling, where we show our superiority over the state-of-the-art supervised / unsupervised
 127 methods.
 128

2. Related Work

130 **Neural Implicit Functions.** Recently, Neural Implicit
 131 Functions (NIFs) have shown promising results in surface
 132 reconstruction [43, 36, 39], novel view synthesis [40, 4, 47],
 133 image super-resolution [48, 41], point normal estimation
 134 [31], etc. In the task of surface reconstruction, the NIFs
 135 approaches train a neural network to represent shapes and
 136 scenes with binary occupancy [39, 46, 14] or signed
 137 distance functions (SDFs) [43, 26, 17, 16, 45, 10, 58, 6], and
 138 then extract surfaces from the learned implicit functions
 139 with the marching cubes algorithm [35]. Previous methods
 140 [39, 43] learn a global latent code for each 3D shape
 141 with a shared MLP to decode geometries. Some advanced
 142 approaches [46, 26] propose to use more latent codes to
 143 represent detailed local geometries. Latest studies bring more
 144 priors learned from large scale datasets to enhance the rep-
 145 resentation ability of NIFs. PCP [38] introduces the pre-
 146 dictive context priors to represent large-scale point clouds.
 147 OnSurf [37] explores the on-surface prior to reconstruct
 148 smooth surfaces from sparse point clouds.
 149

150 NeRF [40] and the following studies [41, 44, 49] ex-
 151 tends NIFs to the task of novel view synthesis. NeuS [53],
 152 VolSDF [55] and Unisurf [42] advance the rendering pro-
 153 cedure of NeRF for surface reconstruction from multi-view
 154 images. ManhattanSDF [22] leverages the manhattan as-
 155 sumption for representing indoor scenes. NeuRIS [51] and
 156 MonoSDF [60] brings the depth prior and normal prior for
 157 improving the surface quality.
 158

159 Occupancy and SDFs are merely suitable to represent
 160 closed shapes. Recently, researchers explore the neural un-
 161 signed distances (UDFs) [15, 62, 61, 50, 13, 52, 34] to re-
 162 present shapes with arbitrary topology. NDF [15] trains a
 163 neural network to learn UDFs with the ground truth distance
 164 values. GIFS [56] jointly learns UDFs and the relationship
 165 of queries. MeshUDF [21] propose a differentiable meshing
 166 algorithm for UDF. However, all the previous UDF-based
 167 methods fail to reconstruct smooth and continuous surfaces
 168 with high-fidelity details due to the disability of learning an
 169 accurate and smooth zero level set of UDF.
 170

171 **Implicit Learning from Raw Point Clouds.** With the
 172 ground truth signed/unsigned distances or occupancy labels
 173 as supervision, previous methods learn NIFs as a regression
 174 [15, 43] problem or classification [39] problem. However,
 175 these expensive supervisions come from the ground truth
 176 meshes which are hard to collect. Moreover, such methods
 177 also fail to generalize to unseen cases with large geo-
 178 metry variations to the training data, which limits the appli-
 179 cation scenarios of such methods. To learn implicit repre-
 180 sentations directly from raw point clouds without ground
 181 truth supervisions, current methods explore the supervision
 182 from sign agnostic [2, 3] learning with gradient constraints
 183 [19]. Neural-Pull [36] employs a new learning schema to
 184 pull space onto surfaces for optimizing SDFs.
 185

186 Latest work CAP-UDF [62] learns UDF progressively
 187 with a field consistency loss. However, the UDF inferred by
 188 CAP-UDF are not accurate and the gradients are unreliable,
 189 especially in the zero level set which indicates the location
 190 of 3D geometries. The key problem is that the differential
 191 neural networks struggle from learning non-differentiable
 192 zero level set of UDF, leading to highly fragmented and
 193 discontinuous surfaces. Since the non-zero level sets of
 194 UDF are all differentiable, we propose to pull the non-zero
 195 level sets onto the zero level set with gradient constraints
 196 which align gradients and correct unsigned distance errors
 197 on the zero level set, leading to a smoother and more con-
 198 tinuous zero level set of unsigned distance field. Our learning
 199 schema involves the constraints for both zero level set and
 200 non-zero level sets of UDF, which differentiates our method
 201 from the previous ones [62, 2, 3, 36, 15, 43].
 202

3. Method

203 **Neural UDFs and Level Sets.** We focus on learning un-
 204 signed distance functions for representing 3D shapes or
 205 scenes with arbitrary typology. Given a raw point cloud
 206 $P = \{p_i \in R^3\}_{i=1}^N$ with N points, we sample a set of
 207 queries $Q = \{q_j \in R^3\}_{j=1}^M$ around P . The UDF f predicts
 208 the unsigned distances s between a query q and the shape
 209 described by P , formulated as:
 210

$$s = f(q). \quad (1)$$

211 A level set S_d of UDF is defined as a region of the 3D
 212 space containing a continuous set of 3D points with the
 213 same unsigned distance d , formulates as:
 214

$$S_d = \{q | f(q) = d\}, \quad (2)$$

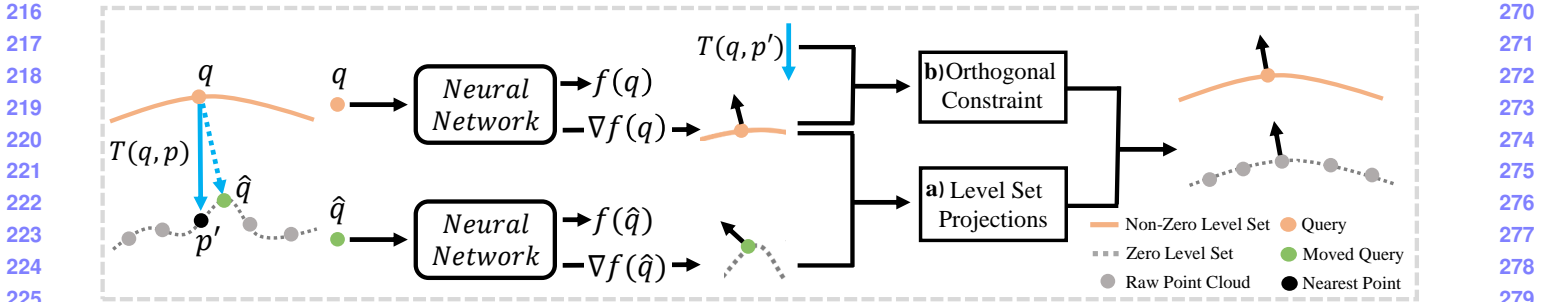


Figure 1. Overview of our method. (a) The level set projection constraint leverages the gradient $\nabla f(q)$ at convincing non-zero level set as the guidance to gradient $\nabla f(\hat{q})$ at unreliable zero level set. (b) The gradient-surface orthogonal constraint encourages the gradients $\nabla f(q)$ at query q orthogonal to the tangent plane of the surface at p' which is the nearest point of q in the raw point cloud.

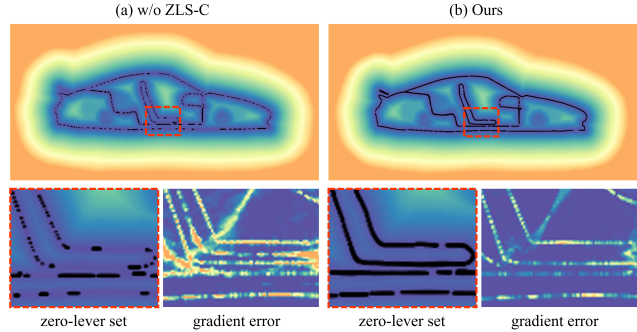


Figure 2. We visualize the fields and the zero level set of UDF learned with or without our designed constraints on the zero level set (ZLS-C). The bluer the color, the smaller the unsigned distances in the field and the errors on gradients.

and the level sets of UDF are defined as $\mathcal{S} = \{S_d\}_{d>=0}$. **Learning UDFs from Point Clouds.** Inspired by CAP-UDF [62], we leverage the pulling optimization for learning UDFs from raw point clouds without ground truth unsigned distances as supervision. Specifically, given a query q_i as input, we move it against the direction of the gradient $g_i = \nabla f(q_i)$ at q_i , the moving operation is formulated as:

$$\hat{q}_i = q_i - f(q_i) \times \nabla f(q_i) / \|\nabla f(q_i)\|_2, \quad (3)$$

where the chamfer distance between moved queries $\hat{Q} = \{\hat{q}_i\}_{i=1}^M$ and the raw point cloud P is calculated as the loss function for optimization, formulated as:

$$\begin{aligned} \mathcal{L}_{CD} &= \frac{1}{M} \sum_{i \in [1, M]} \min_{j \in [1, N]} \|\hat{q}_i - p_j\|_2 \\ &\quad + \frac{1}{N} \sum_{j \in [1, N]} \min_{i \in [1, M]} \|p_j - z_i\|_2, \end{aligned} \quad (4)$$

Zero Level Set of UDF. An accurate zero level set is the key factor for UDF to represent 3D shapes or scenes, since the zero level set indicates the location of 3D geometries. The key problem here is that the differential networks struggle from learning the zero level set where the UDF is not differentiable, which leads to large errors on unsigned distances and gradients around the zero level set.

We provide a visualization of fields and zero level set of UDF learned with neural networks in Fig. 2. As shown in Fig. 2 (a), the zero level set of UDF learned without proper constraints is highly fragmentary and discontinuous with large errors on the gradients at the space near to the zero level set. On the contrary, we achieve the accurate and continuous zero level set as shown in Fig. 2 (b) by introducing level set projection constraint and gradient-surface orthogonal constraint to the zero level set.

Level Set Projections. For learning accurate zero level set of UDF, we design level set projection constraint to guide the learning of zero level set using the rest non-zero level sets. Our idea comes from the observation that despite the unreliable zero level set, the other level sets of the learned UDF are quite convincing, which can serve as the guidance to the field optimization on the zero level set. As shown in Fig. 2, the gradient errors on the non-zero level set are much less than the errors on the zero level set.

We illustrate our method in Fig. 1, where we pull the non-zero level set onto the zero level set with gradient constraints which align gradients and correct unsigned distance errors on the zero level set. We achieve this by encouraging the parallelism between the gradient at queries $Q = \{q_i\}_{i=1}^M$ and the gradient at their projections $\hat{Q} = \{\hat{q}_i\}_{i=1}^M$ to the zero level set, formulated as:

$$\mathcal{L}_{proj} = \frac{1}{M} \sum_{i=1}^M \gamma_i (1 - |\frac{\nabla f(q_i) \cdot \nabla f(\hat{q}_i)}{\|\nabla f(q_i)\|_2 \cdot \|\nabla f(\hat{q}_i)\|_2}|), \quad (5)$$

where γ_i is the factor for weighting the gradient constraint at the query q_i , indicating the importance of optimizing query q_i , formulated as:

$$\gamma_i = \exp(-\lambda |f(q_i)|). \quad (6)$$

We set γ to increase when queries are closer to the zero level set where λ is a hyper-parameter to control the increasing speed. The nonuniform weighting encouraging the network to focus more on the optimizations near the zero level set of UDF.

While \mathcal{L}_{proj} can provide an effective guidance to the gradients at zero level set, we further explore a more accurate

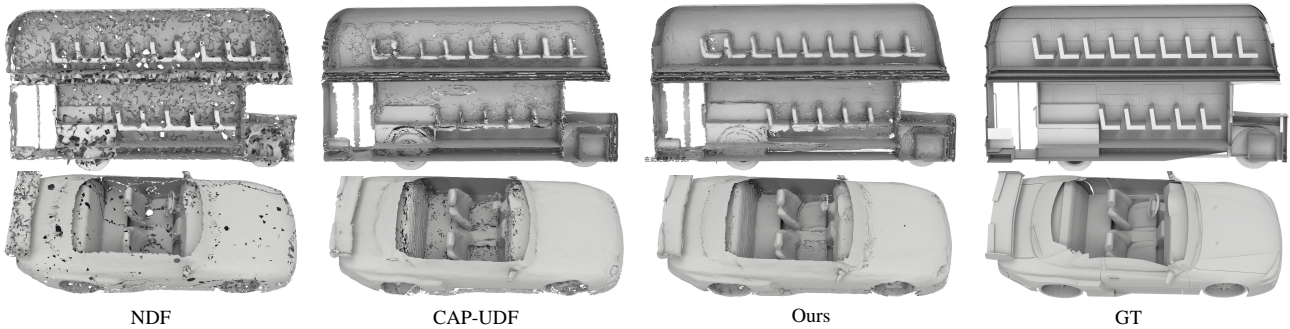


Figure 3. Visual comparisons of surface reconstruction on ShapeNet dataset.

Method	Chamfer-L2		F-Score		NC
	Mean	Median	$F1^{0.005}$	$F1^{0.01}$	
Input	0.363	0.355	48.50	88.34	-
Watertight GT	2.628	2.293	68.82	81.60	-
GT	0.076	0.074	95.70	99.99	-
NDF [15]	0.202	0.193	77.40	97.97	79.1
GIFS [56]	0.128	0.123	88.05	99.31	-
CAP-UDF _{BPA}	0.141	0.138	84.84	99.33	81.8
CAP-UDF	0.119	0.114	88.55	99.82	82.5
Ours	0.098	0.097	92.18	99.90	85.0

Table 1. Surface reconstruction for point cloud on ShapeNet cars dataset (Chamfer-L2 $\times 10^4$).

unsigned distance constraint for correcting the distance values at the zero level set of UDF. The implemented loss is defined as:

$$\mathcal{L}_{\text{dist}} = \frac{1}{N} \sum_{i=1}^N |f(p_i)|, \quad (7)$$

where $p_i \in P$ is the raw point cloud indicating the exact surface to be represented.

Gradient-Surface Orthogonal Constraint. The key idea to guide the learning of zero level set using the rest level sets is based on the observation that the non-zero level sets are much more reliable. To bring a more robust guidance to the optimization of zero level set, we introduce an addition gradient constraint on queries to learn a more stable and regular level sets at the non-zero level sets of UDF by enforcing the gradient orthogonal to the tangent plane of the surface. We design a novel loss to encourage the consistency between the gradient direction at a query q_i and the direction from q_i to its closest point p_i on P , formulated as:

$$\mathcal{L}_{\text{orth}} = \frac{1}{M} \sum_{i=1}^M \left(1 - \left| \frac{\nabla f(q_i) \cdot T(q_i, p_i)}{\|\nabla f(q_i)\|_2 \cdot \|T(q_i, p_i)\|_2} \right| \right), \quad (8)$$

where $T(q_i, p_i)$ is the direction from q_i to p_i . The constraint is illustrated in Fig. 1.

A more naive way of introducing the direction vector $T(q_i, p_i)$ for learning is to explicitly substitute the gradient $\nabla f(q_i)$ with the direction vector $T(q_i, p_i)$, as proposed in

GenSDF [16]. However, $T(q_i, p_i)$ is obviously not the exact direction for q_i to reach the approximated surface since the raw point cloud is the discrete representation of the surface, and p_i is not the exact nearest points of q_i in the approximated surface, which leads to wrong supervisions for GenSDF.

On the contrary, We introduce a more flexible way by treating direction vector $T(q_i, p_i)$ as an optimization objective, which enables the networks to accommodate the inconsistency between the closest point p_i on P and the closest point \hat{q}_i predicted by the networks.

Loss Function. Finally, our loss function is formulated as:

$$\mathcal{L} = \mathcal{L}_{\text{CD}} + \alpha_1 \mathcal{L}_{\text{proj}} + \alpha_2 \mathcal{L}_{\text{dist}} + \alpha_3 \mathcal{L}_{\text{orth}}, \quad (9)$$

where α_1 , α_2 and α_3 are the balance weights for our designed three losses to learn accurate zero level set of UDF.

Applications. The zero level set of UDF indicates the location of represented 3D geometries. Thus, a well-learned UDF with accurate and continuous zero level set can be adopted to different 3D applications.

Surface Reconstruction. Following previous methods [62, 21], the surfaces can be extracted from the zero level set of UDF by judging gradient directions, formulated as:

$$\mathcal{D}(q_i, q_j) = \nabla f(q_i) \cdot \nabla f(q_j), \quad (10)$$

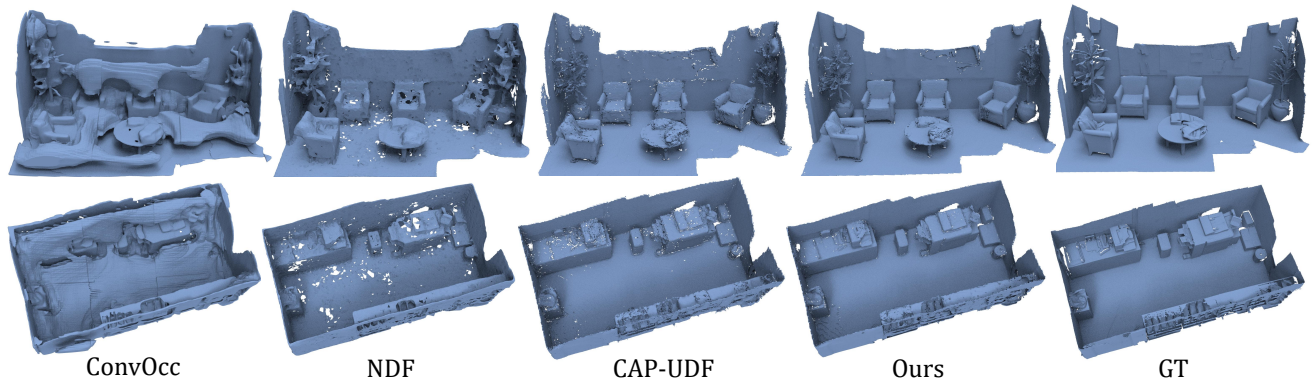
to classify whether two queries q_1 and q_2 are in the same $\mathcal{D}(q_i, q_j) > 0$ or the opposite side $\mathcal{D}(q_i, q_j) < 0$ of the approximated surface. The marching cubes-like algorithm is then used to extract surfaces.

Unsupervised Point Normal Estimation. With a well learned zero level set, we compute the gradients at the raw point clouds P as their estimated normals, formulated as:

$$\mathcal{N}(P) = \{\nabla f(p)\}, p \in P. \quad (11)$$

Unsupervised Point Cloud Upsampling. We randomly sample queries around P , and then move them to the zero level set with Eq. 3 as the upsampled points of P . We further filter the queries with unsigned distance values larger than a threshold β for avoiding outliers. The procedure for upsampling P with a factor of G is formulated as:

$$\mathcal{U}(P) = \{\hat{q}_i, i \in [1, N \times G] | f(q_i) < \beta\} \quad (12)$$

Figure 4. Visual comparisons of surface reconstruction on 3D Scene dataset. Input contains 1K points / m^2

		Burgers			Lounge			Copyroom			Stonewall			Totempole		
		L2CD	L1CD	NC												
500/ m^2	ConvONet [46]	26.97	0.081	0.905	9.044	0.046	0.894	10.08	0.046	0.885	17.70	0.063	0.909	2.165	0.024	0.937
	LIG [26]	3.080	0.046	0.840	6.729	0.052	0.831	4.058	0.038	0.810	4.919	0.043	0.878	9.38	0.062	0.887
	DeepLS [12]	0.714	0.020	0.923	10.88	0.077	0.814	0.552	0.015	0.907	0.673	0.018	0.951	21.15	0.122	0.927
	NDF [15]	0.546	0.018	0.917	0.314	0.012	0.921	0.242	0.012	0.907	0.226	0.012	0.949	1.049	0.025	0.939
	OnSurf [37]	0.609	0.018	0.930	0.529	0.013	0.926	0.483	0.014	0.908	0.666	0.013	0.955	2.025	0.041	0.954
	CAP-UDF [62]	0.192	0.011	0.911	0.099	0.009	0.911	0.120	0.009	0.902	0.069	0.008	0.958	0.131	0.010	0.954
1000/ m^2	Ours	0.161	0.009	0.916	0.087	0.006	0.933	0.102	0.007	0.920	0.061	0.007	0.964	0.114	0.007	0.960
	ConvONet [46]	27.46	0.079	0.907	9.54	0.046	0.894	10.97	0.045	0.892	20.46	0.069	0.905	2.054	0.021	0.943
	LIG [26]	3.055	0.045	0.835	9.672	0.056	0.833	3.61	0.036	0.810	5.032	0.042	0.879	9.58	0.062	0.887
	DeepLS [12]	0.401	0.017	0.920	6.103	0.053	0.848	0.609	0.021	0.901	0.320	0.015	0.954	0.601	0.017	0.950
	NDF [15]	1.168	0.027	0.901	0.393	0.014	0.910	0.269	0.013	0.908	0.509	0.019	0.936	2.020	0.036	0.922
	OnSurf [37]	1.339	0.031	0.929	0.432	0.014	0.934	0.405	0.014	0.914	0.266	0.014	0.957	1.089	0.029	0.954
	CAP-UDF [62]	0.191	0.010	0.910	0.092	0.008	0.927	0.113	0.009	0.911	0.066	0.007	0.962	0.139	0.009	0.955
	Ours	0.146	0.009	0.921	0.068	0.006	0.941	0.093	0.007	0.925	0.050	0.005	0.970	0.107	0.007	0.960

Table 2. Surface reconstruction for point clouds under 3D Scene. L2CD×1000.

4. Experiments

For evaluating the performance of our method, we conduct experiments on surface reconstruction from raw point clouds of shapes (Sec. 4.1), room-level scenes (Sec. 4.2), and real scans (Sec. 4.4), where we also show our results on large-scale driving scenes obtained by fusing LiDAR depths in Sec. 4.3. We further explore the ability of our learned UDF with accurate zero level set for unsupervised point normal estimation (Sec. 4.5) and unsupervised point upsampling (Sec. 4.6). Finally, we conduct ablation studies in Sec. 4.7.

4.1. Surface Reconstruction for Shapes

Dataset and Metrics. To explore the ability of our method in representing shapes with arbitrary topology, we follow previous methods [62, 56] to conduct experiments on the “Car” category of ShapeNet dataset which contains the largest number of shapes with multi-layer structures or open surfaces. We sample 10K points per shape as the input for surface reconstruction. For evaluating the performances, we follow the common setting [56] to sample 100K points from the reconstructed surfaces and leverage Chamfer Distance, Normal Consistency [39] and F-score with a threshold of 0.005 / 0.01 as the evaluation metrics.

Comparisons. We compare our method with the state-of-the-art shape reconstruction methods NDF [15], GIFS [56] and CAP-UDF [62]. We report the quantitative comparison results in Tab. 1, where “Watertight GT” is the result of sampling points from the watertight ground truth, indicating the best performance of the methods base on SDF or occupancy. We also show the superior limit of the dataset by sampling points on the ground truth mesh and report the result as “GT”. Tab. 1 shows that our method achieves the best performance over all the baselines in terms of all metrics. The visual comparison in Fig. 3 further shows that our methods produce more continuous and accurate geometries over all baselines.

4.2. Surface Reconstruction for Room-Level Scenes

Dataset and Metrics. We further explore our performance on real scene scans to demonstrate the ability of our methods to scale to large-scale point clouds. Following On-Surf [37], we conduct experiments on the 3D Scene dataset consisting of complex scenes with open surfaces and scan noises. The input point cloud is achieved by sampling 500 or 1000 points per m^2 uniformly for each scene. We follow the common setting [37, 62] to sample 1M points on both the reconstructed and the ground truth meshes. We leverage L1 / L2 Chamfer Distance and Normal Consistency as the

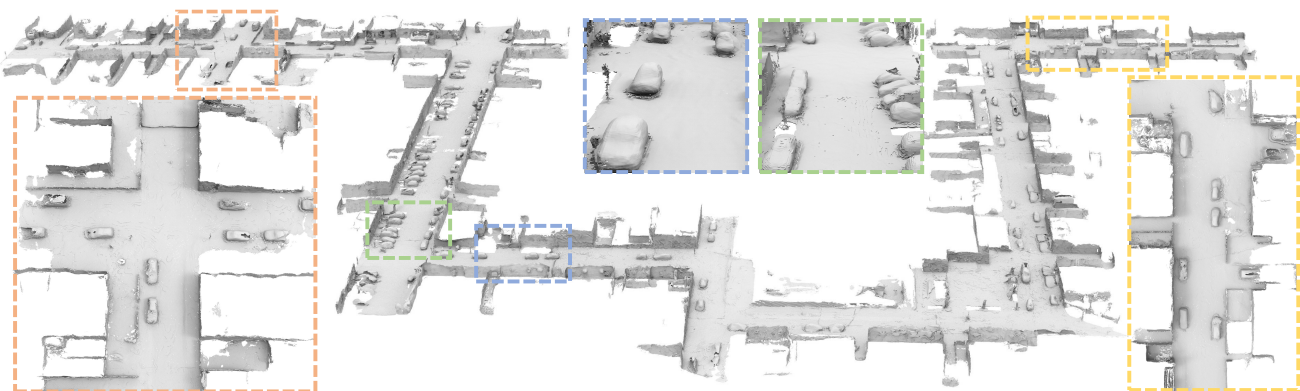


Figure 5. Surface reconstruction results on KITTI odometry dataset (Sequence 00, frame 3000 to 4000).

evaluation metrics.

Comparisons. With different point densities, we compare our method with the state-of-the-art methods ConvONet [46], LIG [26], DeepLS [12], OnSurf [37], NDF [15] and CAP-UDF [62]. The numerical comparison in Tab. 2 demonstrates our superior performance in all scenes. We further present a visual comparison in Fig. 4, where the input point clouds contains $1K$ points/ m^2 . The visualization further shows that our method can reconstruct more detailed and smooth surfaces in complex scenes, where the other UDF-base methods NDF and CAP-UDF produce fragmented surfaces.

4.3. Large-Scale Driving Scene Reconstruction

Dataset. To further demonstrate our scalability to extremely large scenes, we follow NGS [25] to apply our method to KITTI dataset [18]. We use the LiDAR scans of frame 3000 to 4000 in Squeeze00 subset of KITTI dataset as the full input, which are transformed into world coordinates using the provided camera trajectories. We leverage the slide-window strategy to divide the full scene into 15 blocks of size $51.2m^3$, where we sample 300K points per block as the local input to train our network. The final scene is achieved by blending the reconstructed local scenes.

Analysis. The reconstruction results under KITTI scenes is shown in Fig. 5, where our method reproduces visually appealing performances with accurate geometries. Note that: 1) The LiDAR scans contain large amount of noises, especially in the difficult driving scenes. 2) Our method learns to reconstruct surfaces directly from the raw point cloud without learning priors from large-scale datasets.

4.4. Surface Reconstruction for Real Scans

Dataset and Metrics. We demonstrate our advantages for surface reconstruction from real scans by conducting experiments on the Surface Reconstruction Benchmarks [54] (SRB). We follow previous methods [45, 62] to leverage Chamfer Distance and F-Score with a threshold of 1% for evaluation. Note that the ground truth of SRB dataset is



Figure 6. Visual comparisons of surface reconstruction on SRB dataset. SRB dataset provides only point clouds as GT.

dense point cloud containing millions of points. For a comprehensive comparison on the reconstruction quality, we further evaluate the Normal Consistency by first converting the ground truth into meshes with BPA [8] algorithm.

Comparisons. We first report our numerical comparison under SRB dataset with the classic and learning-based methods in Tab. 3. The compared methods include IGR [19], Point2Mesh [23], Screened Poisson Surface Reconstruction (SPSR) [27], Shape As Points (SAP) [45], Neural-Pull [36], NDF [15] and CAP-UDF [62]. Our method achieves the best performance in all metrics as shown in Tab. 3. The visual comparison in Fig. 6 further shows that our methods produce more accurate and smooth geometries over all baselines.

Method	Chamfer-L1	F-Score	NC
IGR [19]	0.178	75.5	86.9
Point2Mesh [23]	0.116	64.8	-
SPSR [27]	0.232	73.5	-
SAP [45]	0.076	83.0	88.6
Neural-Pull [36]	0.106	79.7	87.2
NDF	0.238	68.6	80.4
CAP-UDF	0.073	84.5	88.6
Ours	0.071	85.1	91.0

Table 3. Surface reconstruction for point cloud on SRB dataset.

4.5. Unsupervised Point Normal Estimation

Dataset and Metrics. We adopt the widely-used PCPNet [20] dataset to evaluate our method on the task of point nor-

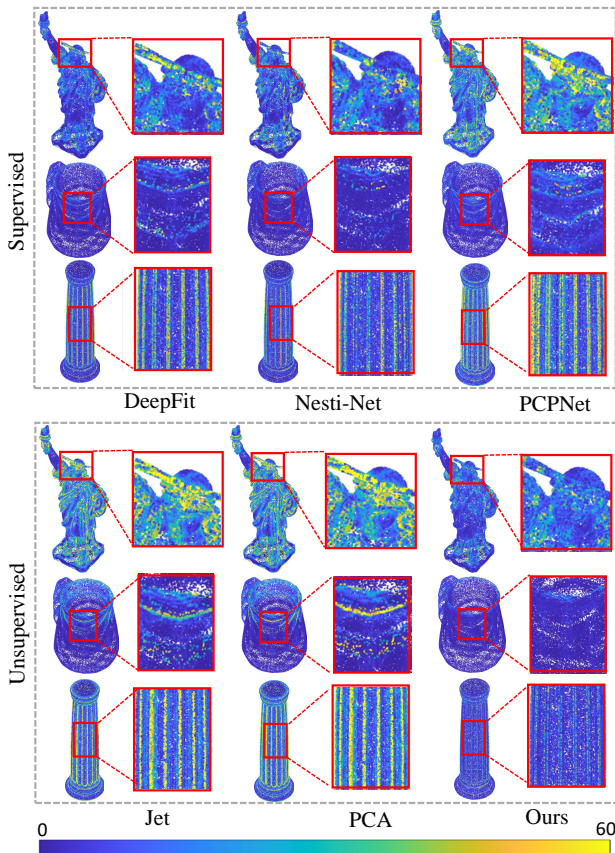


Figure 7. Visual comparisons on error maps of point normal estimation on PCPNet dataset.

	Method	Clean	Strip	Gradient	average
Supervised	PCPNet [20]	9.66	11.47	13.42	11.61
	Hough [9]	10.23	12.47	11.02	11.24
	Nesti-Net [7]	6.99	8.47	9.00	8.15
	IterNet [28]	6.72	7.73	7.51	7.32
	DeepFit [5]	6.51	7.92	7.31	7.25
Unsupervised	Jet [11]	12.23	13.39	13.13	12.92
	PCA [1]	12.29	13.66	12.81	12.92
	Ours (w/o ZLS-c)	7.30	7.74	7.78	7.61
	Ours	6.51	7.45	7.64	7.20

Table 4. Point normal estimation results on the PCPNet dataset.

mal estimation. Each point cloud in the PCPNet dataset contains 100K points. We conduct experiments under three different settings. The inputs of “Clean” setting are sampled uniformly on shapes, and two additional settings with varying point densities (Stripes and Gradients) are added to explore our performance in handling irregular data. Following previous methods [5, 20], we sample 5000 points per shape and compute the angle root mean square error (RMSE) between the predicted normals and the ground truth normals as the evaluation metrics.

Comparisons. We conduct a comparison with traditional

Method	Supervised?	P2F	CD	HD	
PU-Net [59]	Yes	6.84	0.72	8.94	702
MPU [57]	Yes	3.96	0.49	6.11	703
PU-GAN [29]	Yes	2.33	0.28	4.64	704
Dis-PU [30]	Yes	2.01	0.22	2.83	705
EAR [24]	No	5.82	0.52	7.37	706
L2G-AE [32]	No	39.37	6.31	63.23	707
SPU-Net (Tr2T) [33]	No	5.97	0.38	2.24	708
SPU-Net (All2T)	No	5.79	0.37	2.55	709
SPU-Net (Te2T)	No	6.85	0.41	2.18	710
Ours (w/o ZLS-C)	No	1.43	0.24	2.16	711
Ours	No	1.02	0.19	1.55	712

Table 5. Point cloud upsampling results on the PU-GAN dataset.

normal estimation methods including PCA [1], Jets [11] and the state-of-the-art learning-based methods PCPNet [20], HoughCNN [9], Nesti-Net [7], Iter-Net [28] and DeepFit [5]. Note that all the previous learning-based methods are designed in a supervised manner which requires a large scale dataset for training, while we extract normals directly from the unsigned distance fields learned from raw point cloud in an unsupervised way. The numerical results in Tab. 4 show that our method achieves a comparable or even better performance than the state-of-the-art supervised methods. The results also show the effectiveness of our method where the performance degrades from 7.20 to 7.61 without our constraints. The visual comparison in Fig. 7 shows that our method produce more accurate estimations compared to other methods, especially on the complex geometries.

4.6. Unsupervised Point Cloud Upsampling

Dataset and Metrics. For the task of point cloud upsampling, we follow previous methods [33, 30] to conduct experiments on the dataset provided by PU-GAN [29]. We evaluate our method under the setting to generate 8,198 points for each sparse input with 2,048 points. We adopt Chamfer Distance (CD), Hausdorff Distance (HD) and Point-to-Surface distance (P2F) as the evaluation metrics.

Comparisons. We compare our method with the state-of-the-art supervised methods PU-Net [59], MPU [57], PU-GAN [29], Dis-PU [30] and unsupervised methods EAR [24], L2G-AE [32] and SPU-Net [33]. The quantitative comparison is shown in Tab. 5, where our method outperforms the previous supervised and unsupervised methods significantly. The results also show the effectiveness of our method where the performance degrades from 1.55 to 2.16 in terms of HD without our designed constraints. The visualization in Fig. 8 further shows that our upsampling results are more smooth and uniform even compared with the state-of-the-art supervised methods.

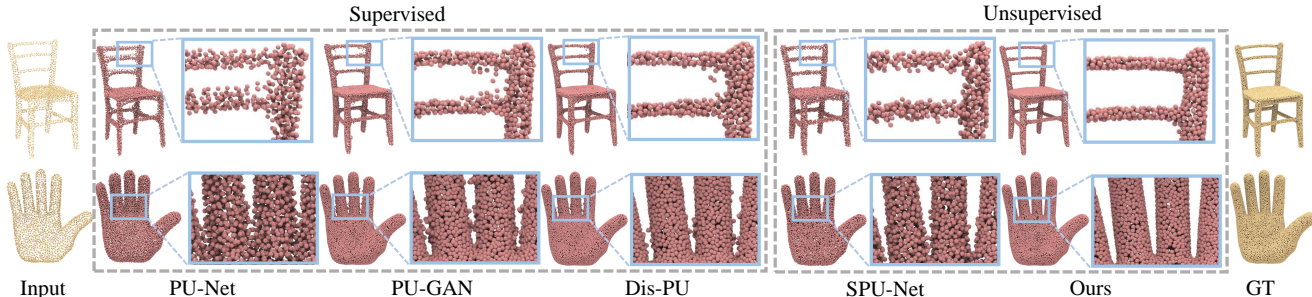
756
757
758
759
760
761
762
763
764
765
766
767

Figure 8. Visual comparisons of point cloud upsampling on PU-GAN dataset.

4.7. Ablation Studies

We conduct ablation studies to demonstrate the effectiveness of each proposed constraint and explore the effect of some important hyper-parameters. We report the performance under a subset of ShapeNet Cars dataset in terms of L2 Chamfer Distance ($\times 10^4$) and Normal Consistency. **Effect of each Design.** We first justify the effectiveness of each proposed constraint in Tab. 6. We report the performance without all the three designed losses as “w/o ZLS-C”. We explore each loss by reporting the results without level set projection loss as “w/o $\mathcal{L}_{\text{proj}}$ ”, surface unsigned distance loss as “w/o $\mathcal{L}_{\text{dist}}$ ”, gradient-surface orthogonal loss as “w/o $\mathcal{L}_{\text{orth}}$ ” and adaptive point weight as “w/o AW”. We replace our level set projection constraint with the GenSDF-style [16] optimization as “GenSDF-Style”. We further constrain the level set projection loss on a randomly selected non-zero level set other than the zero level set and report the performance as “Non-zero LSC”. The result demonstrates that the zero level set is the key factor that influence the representation ability of UDF.

	w/o ZLS-C	w/o $\mathcal{L}_{\text{proj}}$	w/o $\mathcal{L}_{\text{dist}}$	w/o $\mathcal{L}_{\text{orth}}$
L2CD	0.126	0.107	0.101	0.096
NC	82.7	82.9	83.9	84.1
	w/o AW	GenSDF-Style	Non-zero LSC	Ours
L2CD	0.096	0.101	0.098	0.091
NC	84.2	83.9	83.5	84.4

Table 6. Effect of framework design.

Weight of Level Set Projection Loss. We report the performance with different weights of the level set projection loss $\mathcal{L}_{\text{proj}}$ in Tab. 7. We found that a suitable weight of $\mathcal{L}_{\text{proj}}$ will improve the reconstruction accuracy, and it may affect the optimization to converge if we weight too much.

	0.001	0.002	0.01	0.1
L2CD	0.095	0.091	0.162	0.359
NC	84.2	84.4	83.4	79.6

Table 7. Weight of level set projection loss.

Weight of Surface Unsigned Distance Loss. We further explore the effect of weights α_2 for the surface unsigned distance loss in Tab 8, where we found that a too large or too small weight will degenerate the performance.

	0.001	0.01	0.1	1
L2CD	0.101	0.100	0.091	0.449
NC	84.1	84.1	84.4	78.9

Table 8. Weight of surface unsigned distance loss.

Weight of Gradient-Surface Orthogonal Loss. We evaluate the effect of the weight α_3 for gradient-surface orthogonal loss in Tab. 9. A proper weight $\alpha_3 = 0.01$ brings the best improvement while a too much weight will affect the convergence.

	0.001	0.01	0.1	1
L2CD	0.094	0.091	0.335	2.55
NC	84.2	84.4	77.7	72.9

Table 9. Weight of gradient-surface orthogonal loss.

Effect of Adaptive per Point Weights. We further report the performance under different λ which controls the increasing speed of adaptive weights for each point in Tab. 10. We found that λ has a relative small impact on the Chamfer Distance with large affect on the Normal Consistency, which indicates that the adaptive per point weight can improve the surface smoothness.

	1	10	100	1000
L2CD	0.093	0.091	0.092	0.094
NC	84.1	84.4	83.7	83.2

Table 10. Effect of adaptive per point weights.

5. Conclusion

In this paper, we justify that an accurate and continuous zero level set of unsigned distance functions is the key factor to represent complex 3D geometries. We therefore propose two novel constraints on UDF to achieve a more continuous zero level set by projecting non-zero level set to guide the optimization of zero level set. With the ability of learning consistent and accurate zero level set of UDF, we explore three different 3D applications including surface reconstruction, unsupervised point normal estimation and unsupervised point cloud upsampling, where the visual and numerical comparisons with the state-of-the-art supervised/unsupervised methods justify our effectiveness and show our superiority over the latest methods.

864
865
866
867
868
869
870
871
872
873
874
875
876
877
878
879
880
881
882
883
884
885
886
887
888
889
890
891
892
893
894
895
896
897
898
899
900
901
902
903
904
905
906
907
908
909
910
911
912
913
914
915
916
917

References

- [1] Hervé Abdi and Lynne J Williams. Principal component analysis. *Wiley Interdisciplinary Reviews: Computational Statistics*, 2(4):433–459, 2010. 7
- [2] Matan Atzmon and Yaron Lipman. SAL: Sign agnostic learning of shapes from raw data. In *Proceedings of the IEEE/CVF Conference on Computer Vision and Pattern Recognition*, pages 2565–2574, 2020. 2
- [3] Matan Atzmon and Yaron Lipman. SALD: Sign agnostic learning with derivatives. In *International Conference on Learning Representations*, 2020. 2
- [4] Jonathan T Barron, Ben Mildenhall, Matthew Tancik, Peter Hedman, Ricardo Martin-Brualla, and Pratul P Srinivasan. Mip-nerf: A multiscale representation for anti-aliasing neural radiance fields. In *Proceedings of the IEEE/CVF International Conference on Computer Vision*, pages 5855–5864, 2021. 2
- [5] Yizhak Ben-Shabat and Stephen Gould. DeepFit: 3d surface fitting via neural network weighted least squares. In *European Conference on Computer Vision*, pages 20–34. Springer, 2020. 7
- [6] Yizhak Ben-Shabat, Chamin Hewa Koneputugodage, and Stephen Gould. Digs: Divergence guided shape implicit neural representation for unoriented point clouds. In *Proceedings of the IEEE/CVF Conference on Computer Vision and Pattern Recognition*, pages 19323–19332, 2022. 2
- [7] Yizhak Ben-Shabat, Michael Lindenbaum, and Anath Fischer. Nesti-Net: Normal estimation for unstructured 3d point clouds using convolutional neural networks. In *Proceedings of the IEEE/CVF Conference on Computer Vision and Pattern Recognition*, pages 10112–10120, 2019. 7
- [8] Fausto Bernardini, Joshua Mittleman, Holly Rushmeier, Cláudio Silva, and Gabriel Taubin. The ball-pivoting algorithm for surface reconstruction. *IEEE Transactions on Visualization and Computer Graphics*, 5(4):349–359, 1999. 6
- [9] Alexandre Boulch and Renaud Marlet. Deep learning for robust normal estimation in unstructured point clouds. In *Computer Graphics Forum*, volume 35, pages 281–290. Wiley Online Library, 2016. 7
- [10] Alexandre Boulch and Renaud Marlet. POCO: Point convolution for surface reconstruction. In *Proceedings of the IEEE/CVF Conference on Computer Vision and Pattern Recognition*, pages 6302–6314, 2022. 2
- [11] Frédéric Cazals and Marc Pouget. Estimating differential quantities using polynomial fitting of osculating jets. *Computer Aided Geometric Design*, 22(2):121–146, 2005. 7
- [12] Rohan Chabra, Jan E Lenssen, Eddy Ilg, Tanner Schmidt, Julian Straub, Steven Lovegrove, and Richard Newcombe. Deep local shapes: Learning local sdf priors for detailed 3D reconstruction. In *European Conference on Computer Vision*, pages 608–625. Springer, 2020. 1, 5, 6
- [13] Weikai Chen, Cheng Lin, Weiyang Li, and Bo Yang. 3psdf: Three-pole signed distance function for learning surfaces with arbitrary topologies. In *Proceedings of the IEEE/CVF Conference on Computer Vision and Pattern Recognition*, pages 18522–18531, 2022. 2
- [14] Zhiqin Chen and Hao Zhang. Learning implicit fields for generative shape modeling. In *Proceedings of the IEEE/CVF Conference on Computer Vision and Pattern Recognition*, pages 5939–5948, 2019. 2
- [15] Julian Chibane, Gerard Pons-Moll, et al. Neural unsigned distance fields for implicit function learning. *Advances in Neural Information Processing Systems*, 33:21638–21652, 2020. 1, 2, 4, 5, 6
- [16] Gene Chou, Ilya Chugunov, and Felix Heide. Gensdf: Two-stage learning of generalizable signed distance functions. In *Advances in Neural Information Processing Systems*. 2, 4, 8
- [17] Yueqi Duan, Haidong Zhu, He Wang, Li Yi, Ram Nevatia, and Leonidas J Guibas. Curriculum deep sdf. In *European Conference on Computer Vision*, pages 51–67. Springer, 2020. 2
- [18] Andreas Geiger, Philip Lenz, and Raquel Urtasun. Are we ready for autonomous driving? the kitti vision benchmark suite. In *2012 IEEE conference on computer vision and pattern recognition*, pages 3354–3361. IEEE, 2012. 6
- [19] Amos Gropp, Lior Yariv, Niv Haim, Matan Atzmon, and Yaron Lipman. Implicit geometric regularization for learning shapes. In *International Conference on Machine Learning*, pages 3789–3799. PMLR, 2020. 2, 6
- [20] Paul Guerrero, Yanir Kleiman, Maks Ovsjanikov, and Niloy J Mitra. PCPNet: learning local shape properties from raw point clouds. In *Computer Graphics Forum*, volume 37, pages 75–85. Wiley Online Library, 2018. 1, 6, 7
- [21] Benoit Guillard, Federico Stella, and Pascal Fua. MeshUDF: Fast and differentiable meshing of unsigned distance field networks. *European Conference on Computer Vision*, 2022. 1, 2, 4
- [22] Haoyu Guo, Sida Peng, Haotong Lin, Qianqian Wang, Guofeng Zhang, Hujun Bao, and Xiaowei Zhou. Neural 3d scene reconstruction with the manhattan-world assumption. In *Proceedings of the IEEE/CVF Conference on Computer Vision and Pattern Recognition*, pages 5511–5520, 2022. 2
- [23] Rana Hanocka, Gal Metzger, Raja Giryes, and Daniel Cohen-Or. Point2mesh: a self-prior for deformable meshes. *ACM Transactions on Graphics (TOG)*, 39(4):126–1, 2020. 6
- [24] Hui Huang, Shihao Wu, Minglun Gong, Daniel Cohen-Or, Uri Ascher, and Hao Zhang. Edge-aware point set resampling. *ACM transactions on graphics (TOG)*, 32(1):1–12, 2013. 7
- [25] Jiahui Huang, Hao-Xiang Chen, and Shi-Min Hu. A neural galerkin solver for accurate surface reconstruction. *ACM Transactions on Graphics (TOG)*, 41(6):1–16, 2022. 6
- [26] Chiyu Jiang, Avneesh Sud, Ameesh Makadia, Jingwei Huang, Matthias Nießner, Thomas Funkhouser, et al. Local implicit grid representations for 3D scenes. In *Proceedings of the IEEE/CVF Conference on Computer Vision and Pattern Recognition*, pages 6001–6010, 2020. 2, 5, 6
- [27] Michael Kazhdan and Hugues Hoppe. Screened poisson surface reconstruction. *ACM Transactions on Graphics (TOG)*, 32(3):1–13, 2013. 6
- [28] Jan Eric Lenssen, Christian Osendorfer, and Jonathan Masci. Deep iterative surface normal estimation. In *Proceedings of the IEEE/CVF Conference on Computer Vision and Pattern Recognition*, pages 11247–11256, 2020. 7

- 972 [29] Ruihui Li, Xianzhi Li, Chi-Wing Fu, Daniel Cohen-Or, and
973 Pheng-Ann Heng. Pu-gan: a point cloud upsampling ad-
974 versarial network. In *Proceedings of the IEEE/CVF international*
975 *conference on computer vision*, pages 7203–7212, 2019. 1, 7 1026
- 976 [30] Ruihui Li, Xianzhi Li, Pheng-Ann Heng, and Chi-Wing Fu.
977 Point cloud upsampling via disentangled refinement. In *Pro-
978 ceedings of the IEEE/CVF conference on computer vision and
979 pattern recognition*, pages 344–353, 2021. 7 1027
- 980 [31] Shujuan Li, Junsheng Zhou, Baorui Ma, Yu-Shen Liu, and
981 Zhizhong Han. NeAF: Learning neural angle fields for point
982 normal estimation. In *Proceedings of the AAAI Conference
983 on Artificial Intelligence*, 2023. 2 1028
- 984 [32] Xinhai Liu, Zhizhong Han, Xin Wen, Yu-Shen Liu, and
985 Matthias Zwicker. L2g auto-encoder: Understanding point
986 clouds by local-to-global reconstruction with hierarchical
987 self-attention. In *Proceedings of the 27th ACM International
988 Conference on Multimedia*, pages 989–997, 2019. 7 1029
- 989 [33] Xinhai Liu, Xinchen Liu, Yu-Shen Liu, and Zhizhong Han.
990 SPU-Net: Self-supervised point cloud upsampling by
991 coarse-to-fine reconstruction with self-projection optimiza-
992 tion. *IEEE Transactions on Image Processing*, 31:4213–
993 4226, 2022. 7 1030
- 994 [34] Xiaoxiao Long, Cheng Lin, Lingjie Liu, Yuan Liu, Peng
995 Wang, Christian Theobalt, Taku Komura, and Wenping
996 Wang. Neuraludf: Learning unsigned distance fields for
997 multi-view reconstruction of surfaces with arbitrary topolo-
998 gies. *arXiv preprint arXiv:2211.14173*, 2022. 2 1031
- 999 [35] William E Lorensen and Harvey E Cline. Marching cubes:
1000 A high resolution 3D surface construction algorithm. *ACM
1001 Siggraph Computer Graphics*, 21(4):163–169, 1987. 2 1032
- 1002 [36] Baorui Ma, Zhizhong Han, Yu-Shen Liu, and Matthias
1003 Zwicker. Neural-Pull: Learning signed distance function
1004 from point clouds by learning to pull space onto surface.
1005 In *International Conference on Machine Learning*, pages
1006 7246–7257. PMLR, 2021. 1, 2, 6 1033
- 1007 [37] Baorui Ma, Yu-Shen Liu, and Zhizhong Han. Reconstruct-
1008 ing surfaces for sparse point clouds with on-surface priors.
1009 In *Proceedings of the IEEE/CVF Conference on Computer
1010 Vision and Pattern Recognition*, 2022. 1, 2, 5, 6 1034
- 1011 [38] Baorui Ma, Yu-Shen Liu, Matthias Zwicker, and Zhizhong
1012 Han. Surface reconstruction from point clouds by learning
1013 predictive context priors. In *Proceedings of the IEEE/CVF
1014 Conference on Computer Vision and Pattern Recognition*,
1015 2022. 2 1035
- 1016 [39] Lars Mescheder, Michael Oechsle, Michael Niemeyer,
1017 Sebastian Nowozin, and Andreas Geiger. Occupancy networks:
1018 Learning 3D reconstruction in function space. In *Proceed-
1019 ings of the IEEE/CVF Conference on Computer Vision and
1020 Pattern Recognition*, pages 4460–4470, 2019. 1, 2, 5 1036
- 1021 [40] B Mildenhall, PP Srinivasan, M Tancik, JT Barron, R Ra-
1022 mamoorthi, and R Ng. NeRF: Representing scenes as neural
1023 radiance fields for view synthesis. In *European Conference
1024 on Computer Vision*, 2020. 1, 2 1037
- 1025 [41] Thomas Müller, Alex Evans, Christoph Schied, and Alexander
1026 Keller. Instant neural graphics primitives with a multi-
1027 resolution hash encoding. *ACM Transactions on Graphics
(ToG)*, 41(4):1–15, 2022. 2 1038
- [42] Michael Oechsle, Songyou Peng, and Andreas Geiger.
Unisurf: Unifying neural implicit surfaces and radiance
fields for multi-view reconstruction. In *Proceedings of the
IEEE/CVF International Conference on Computer Vision*,
pages 5589–5599, 2021. 1, 2 1039
- [43] Jeong Joon Park, Peter Florence, Julian Straub, Richard
Newcombe, and Steven Lovegrove. DeepSDF: Learning
continuous signed distance functions for shape representa-
tion. In *Proceedings of the IEEE/CVF Conference on Com-
puter Vision and Pattern Recognition*, pages 165–174, 2019.
1, 2 1040
- [44] Keunhong Park, Utkarsh Sinha, Jonathan T Barron, Sofien
Bouaziz, Dan B Goldman, Steven M Seitz, and Ricardo
Martin-Brualla. Nerfies: Deformable neural radiance fields.
In *Proceedings of the IEEE/CVF International Conference
on Computer Vision*, pages 5865–5874, 2021. 2 1041
- [45] Songyou Peng, Chiyu Jiang, Yiyi Liao, Michael Niemeyer,
Marc Pollefeys, and Andreas Geiger. Shape as points: A dif-
ferentiable poisson solver. *Advances in Neural Information
Processing Systems*, 34, 2021. 2, 6 1042
- [46] Songyou Peng, Michael Niemeyer, Lars Mescheder, Marc
Pollefeys, and Andreas Geiger. Convolutional occupancy
networks. In *European Conference on Computer Vision*,
pages 523–540. Springer, 2020. 1, 2, 5, 6 1043
- [47] Albert Pumarola, Enric Corona, Gerard Pons-Moll, and
Francesc Moreno-Noguer. D-nerf: Neural radiance fields
for dynamic scenes. In *Proceedings of the IEEE/CVF Con-
ference on Computer Vision and Pattern Recognition*, pages
10318–10327, 2021. 2 1044
- [48] Vincent Sitzmann, Julien Martel, Alexander Bergman, David
Lindell, and Gordon Wetzstein. Implicit neural represen-
tations with periodic activation functions. *Advances in Neural
Information Processing Systems*, 33:7462–7473, 2020. 2 1045
- [49] Matthew Tancik, Vincent Casser, Xinchen Yan, Sabeek Prad-
han, Ben Mildenhall, Pratul P Srinivasan, Jonathan T Barron,
and Henrik Kretzschmar. Block-NeRF: Scalable large scene
neural view synthesis. In *Proceedings of the IEEE/CVF Con-
ference on Computer Vision and Pattern Recognition*, pages
8248–8258, 2022. 2 1046
- [50] Rahul Venkatesh, Tejan Karmali, Sarthak Sharma, Auro-
brata Ghosh, R Venkatesh Babu, László A Jeni, and Maneesh
Singh. Deep implicit surface point prediction networks. In
*Proceedings of the IEEE/CVF International Conference on
Computer Vision*, pages 12653–12662, 2021. 2 1047
- [51] Jiepeng Wang, Peng Wang, Xiaoxiao Long, Christian
Theobalt, Taku Komura, Lingjie Liu, and Wenping Wang.
NeuRIS: Neural reconstruction of indoor scenes using nor-
mal priors. In *17th European Conference on Computer Vi-
sion*, pages 139–155. Springer, 2022. 2 1048
- [52] Li Wang, Jie Yang, Weikai Chen, Xiaoxu Meng, Bo Yang,
Jintao Li, and Lin Gao. Hsdf: Hybrid sign and distance field
for modeling surfaces with arbitrary topologies. In *Advances
in Neural Information Processing Systems*. 2 1049
- [53] Peng Wang, Lingjie Liu, Yuan Liu, Christian Theobalt, Taku
Komura, and Wenping Wang. NeuS: Learning neural im-
plicit surfaces by volume rendering for multi-view recon-
struction. *Advances in Neural Information Processing Sys-
tems*, 34:27171–27183, 2021. 1, 2 1050

- 1080 [54] Francis Williams, Teseo Schneider, Claudio Silva, Denis 1134
1081 Zorin, Joan Bruna, and Daniele Panozzo. Deep geometric 1135
1082 prior for surface reconstruction. In *Proceedings of 1136
1083 the IEEE/CVF Conference on Computer Vision and Pattern 1137
1084 Recognition*, pages 10130–10139, 2019. 6 1138
1085 [55] Lior Yariv, Jitao Gu, Yoni Kasten, and Yaron Lipman. 1139
1086 Volume rendering of neural implicit surfaces. *Advances in Neu- 1140
1087 ral Information Processing Systems*, 34:4805–4815, 2021. 2 1141
1088 [56] Jianglong Ye, Yuntao Chen, Naiyan Wang, and Xiaolong 1142
1089 Wang. GIFS: Neural implicit function for general shape 1143
1090 representation. *Proceedings of the IEEE/CVF Conference on 1144
1091 Computer Vision and Pattern Recognition*, 2022. 2, 4, 5 1145
1092 [57] Wang Yifan, Shihao Wu, Hui Huang, Daniel Cohen-Or, and 1146
1093 Olga Sorkine-Hornung. Patch-based progressive 3d point set 1147
1094 upsampling. In *Proceedings of the IEEE/CVF Conference on 1148
1095 Computer Vision and Pattern Recognition*, pages 5958– 1149
1096 5967, 2019. 7 1150
1097 [58] Wang Yifan, Shihao Wu, Cengiz Oztireli, and Olga Sorkine- 1151
1098 Hornung. Iso-points: Optimizing neural implicit surfaces 1152
1099 with hybrid representations. In *Proceedings of the IEEE/CVF Conference 1153
1100 on Computer Vision and Pattern Recognition*, pages 374–383, 2021. 2 1154
1101 [59] Lequan Yu, Xianzhi Li, Chi-Wing Fu, Daniel Cohen-Or, and 1155
1102 Pheng-Ann Heng. Pu-net: Point cloud upsampling network. 1156
1103 In *Proceedings of the IEEE conference on computer vision 1157
1104 and pattern recognition*, pages 2790–2799, 2018. 7 1158
1105 [60] Zehao Yu, Songyou Peng, Michael Niemeyer, Torsten Sattler, 1159
1106 and Andreas Geiger. Monosdf: Exploring monocular 1160
1107 geometric cues for neural implicit surface reconstruction. In 1161
1108 *Advances in Neural Information Processing Systems*. 2 1162
1109 [61] Fang Zhao, Wenhao Wang, Shengcai Liao, and Ling Shao. 1163
1110 Learning anchored unsigned distance functions with gradient 1164
1111 direction alignment for single-view garment reconstruction. 1165
1112 In *Proceedings of the IEEE/CVF International Conference 1166
1113 on Computer Vision*, pages 12674–12683, 2021. 2 1167
1114 [62] Junsheng Zhou, Baorui Ma, Yu-Shen Liu, Yi Fang, and 1168
1115 Zhizhong Han. Learning consistency-aware unsigned 1169
1116 distance functions progressively from raw point clouds. In *Ad- 1170
1117 vances in Neural Information Processing Systems (NeurIPS)*, 1171
1118 2022. 1, 2, 3, 4, 5, 6 1172
1119 1173
1120 1174
1121 1175
1122 1176
1123 1177
1124 1178
1125 1179
1126 1180
1127 1181
1128 1182
1129 1183
1130 1184
1131 1185
1132 1186
1133 1187